

Measurement of the real dielectric permittivity ϵ_r of glacial ice

Allison, P.^{b,c}, Archambault, S.^d, Auffenberg, J.^e, Bard, R.^f, Beatty, J.J.^{b,c}, Beheler-Amass, M.^e, Besson, D.Z.^{a,g}, Beydler, M.^e, Chen, C.C.^h, Chen, C.H.^h, Chen, P.^h, Christenson, A.^e, Clark, B.A.^{b,c}, Connolly, A.^{b,c}, Cremonesi, L.ⁱ, Deaconu, C.^j, Duvernois, M.^e, Friedman, L.^f, Gaior, R.^d, Hanson, J.^{b,c}, Hanson, K.^e, Haugen, J.^e, Hoffman, K.D.^f, Hong, E.^{b,c}, Hsu, S.Y.^h, Hu, L.^h, Huang, J.J.^h, Huang, M.-H. A.^h, Ishihara, A.^d, Karle, A.^e, Kelley, J.L.^e, Khandelwal, R.^e, Kim, M.-C.^d, Kravchenko, I.^k, Kruse, J.^k, Kurusu, K.^d, Kuwabara, T.^d, Landsman, H.^l, Latif, U.A.^a, Laundrie, A.^e, Li, C.-J.^h, Liu, T.-C.^h, Lu, M.-Y.^e, Mase, K.^d, Meures, T.^e, Nam, J.^d, Nichols, R.J.ⁱ, Nir, G.^l, Novikov, A.^{a,g}, Oberla, E.^j, O' Murchadha, A.^e, Pan, Y.^m, Pfendner, C.^{b,c}, Ratzlaff, K.^a, Relich, M.^c, Roth, J.^m, Sandstrom, P.^e, Seckel, D.^m, Shiao, Y.S.^h, Shultz, A.^k, Song, M.^f, Touart, J.^f, Varner, G.S.ⁿ, Vieregge, A.^j, Wang, M.Z.^h, Wang, S.H.^h, Wissel, S.^o, Yoshida, S.^d, Young, R.^a

^aDept. of Physics and Astronomy, Univ. of Kansas, Lawrence, KS, USA

^bDept. of Physics, The Ohio State University, 191 West Woodruff Avenue, Columbus, OH, USA

^cCenter for Cosmology and Astro-Particle Physics, The Ohio State University, 191 West Woodruff Avenue, Columbus, OH, USA

^dDept. of Physics, Chiba University, Tokyo, Japan

^eDept. of Physics and Wisconsin IceCube Particle Astrophysics Center, University of Wisconsin, Madison, WI, USA

^fDept. of Physics, Univ. of Maryland, College Park, MD, USA

^gNational Research Nuclear University, Moscow Engineering Physics Institute, Moscow, Russia

^hDept. of Physics, Grad. Inst. of Astrophys., & Leung Center for Cosmology and Particle Astrophysics, National Taiwan Univ., Taipei, Taiwan

ⁱDept. of Physics and Astronomy, Univ. College London, London, United Kingdom

^jDept. of Physics, University of Chicago, Chicago, IL, USA

^kDept. of Physics and Astronomy, Univ. of Nebraska-Lincoln, NE, USA

^lWeizmann Institute of Science, Rehovot, Israel

^mDept. of Physics and Astronomy, Univ. of Delaware, Newark, DE, USA

ⁿDept. of Physics and Astronomy, Univ. of Hawaii, Manoa, HI, USA

^oDept. of Physics, California Polytechnic State University, San Luis Obispo, CA, USA

Abstract

Owing to their small interaction cross-section, neutrinos are unparalleled astronomical tracers. Ultra-high energy (UHE; $E > 10$ PeV) neutrinos probe the most distant, most explosive sources in the Universe, often obscured to optical telescopes. Radio-frequency (RF) detection of Askaryan radiation in cold polar ice is currently regarded as the best experimental measurement technique for UHE neutrinos, provided the RF properties of the ice target can be well-understood. To that end, the Askaryan Radio Array (ARA) experiment at the South Pole has used long-baseline RF propagation to extract information on the index-of-refraction ($n = \sqrt{\epsilon_r}$) in South Polar ice. Owing to the increasing ice density over the upper 150–200 meters, rays are measured along two, nearly parallel paths, one of which refracts through an inflection point, with differences in both arrival time and arrival angle that can be used to constrain the neutrino properties. We also observe (first) indications for RF ice birefringence for signals propagating along predominantly horizontal trajectories, corresponding to an asymmetry of order 0.1% between the ordinary and extra-ordinary birefringent axes, numerically compatible with previous measurements of birefringent asymmetries for vertically-propagating radio-frequency signals at South Pole. Qualitatively, these effects offer the possibility of redundantly measuring the range from receiver to a neutrino interaction in Antarctic ice, if receiver antennas are deployed at shallow ($z \sim 25$ – 100 m) depths. Such range information is essential in determining both the neutrino energy, as well as the incident neutrino direction.

1. Introduction

The glacial ice in Antarctica offers a unique opportunity for detection of neutrinos. There are currently three Antarctic experiments which seek detection, via the Askaryan effect[1, 2, 3], of UHE neutrinos using the ice sheet as a neutrino target[4]. Hadronic and electromagnetic showers resulting from neutrino collisions with ice molecules acquire, as they evolve, a net negative charge as atomic electrons are Compton scattered into the forward-moving shower and shower positrons depleted via annihilation with atomic electrons, resulting in a coherent, detectable electromagnetic signal at radio wavelength scales, distributed on a Cherenkov cone approximately 1–2 degrees in transverse width, and with half-opening angle $\sim 57^\circ$. Above 10 EeV, the most promising (“cosmogenic”) neutrino source for these experiments[5, 6, 7, 8] results from photoproduction of pions due to interactions of ultra-high energy nucleons with cosmic microwave background (CMB) photons, with subsequent decays to neutrinos. Recent measurements by the IceCube experiment of PeV-scale neutrinos[4] have intensified interest in a large-scale radio array capable of measuring the continuation of that spectrum at higher energies; the observation of the first identified extra-galactic neutrino source has provided additional impetus[9].

The Askaryan Radio Array[10, 11, 12] (ARA) at the South Pole (Figure 1) has proposed multiple, independent stations in a hexagonal array with inter-station spacing of 2 km. Following the initial 2010/11 deployment of a “TestBed”

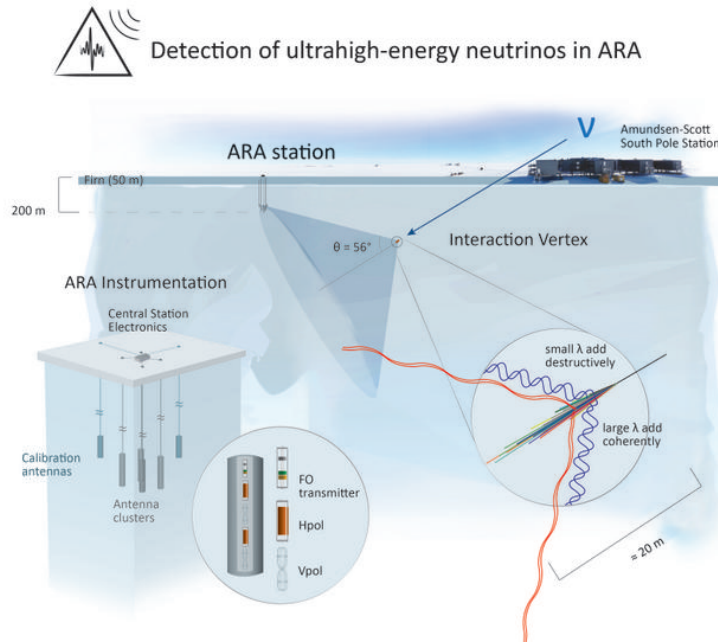


Figure 1: Schematic of ARA neutrino detection, showing the ARA receiver antennas illuminated by radio-frequency Cherenkov signal resulting from an in-ice neutrino interaction.

in the upper 30 meters of the South Polar ice sheet, three more (ARA-1, ARA-2, and ARA-3) stations were deployed in 2011/12 and 2012/13, with two more (ARA-4 and ARA-5) commissioned in 2017/18, including an advanced trigger system exploiting phased array techniques[13] on ARA-5. The analysis described below is based on the pre-2017 station configuration, as shown in Figure 2.

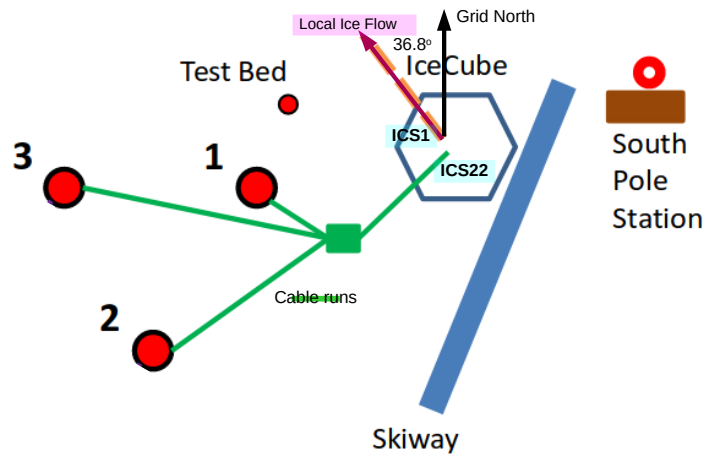


Figure 2: Station geometry for measurements described herein.

Following ARA-1, for which a drill malfunction limited deployment to approximately 40% of the desired 200 meter depth, the subsequent station receivers were deployed at depths of 175-200 m. Each station includes 16 antennas, 8 sensitive to vertically polarized (Vpol) and 8 sensitive to horizontally polarized (Hpol) radiation, with in-ice bandwidths of approximately 150-700 MHz and 250-400 MHz, respectively. Surface antennas, sensitive over the 25–800 MHz regime, deployed on the TestBed, ARA-1, ARA-2 and ARA-3, can be used to monitor low-frequency galactic noise, although they rarely give signals coincident with the in-ice antennas, given the typical time delays in signal arrival times between the surface and the deep station antennas. In-ice antennas are installed on four strings defining the corners of a cuboid approximately 20m in height and 20m along the horizontal diagonal. An H/V pair is located at each corner of the

cuboid, consisting of an Hpol antenna deployed 2m–3m above a Vpol antenna, such that H/V signal arrival times should be synchronous to within 10 ns. Signals are amplified at the antenna, passed by an in-ice RF-over-optical fiber link to the surface, and then converted back to RF voltage signals by a surface optical fiber receiver before entering the data acquisition system. Full station data collection is triggered whenever (3 of 8 Hpol) .OR. (3 of 8 Vpol) antennas exceed some voltage threshold within a time window (170 ns) inclusive to the RF travel time across the station. Thresholds are dynamically adjusted to maintain a combined event trigger rate of 5-7 Hz, comfortably below the saturation data-taking rate of 25 Hz. Following the issue of a valid trigger, signals from all 16 antennas are digitized and stored, with a readout window typically wide enough to include ~ 100 ns of pre-trigger and ~ 300 ns of post-trigger waveform data. A local calibration pulser, approximately 30 meters displaced from the centroid of the receiver array, emits signals at one pulse per second, to monitor receiver performance. For the testbed, received cal pulser signals in both HPol and VPol are presented elsewhere[10]. The response of the vertically-polarized receivers to the local, vertically-polarized cal pulser, for ARA-2 is shown in Figure 3.

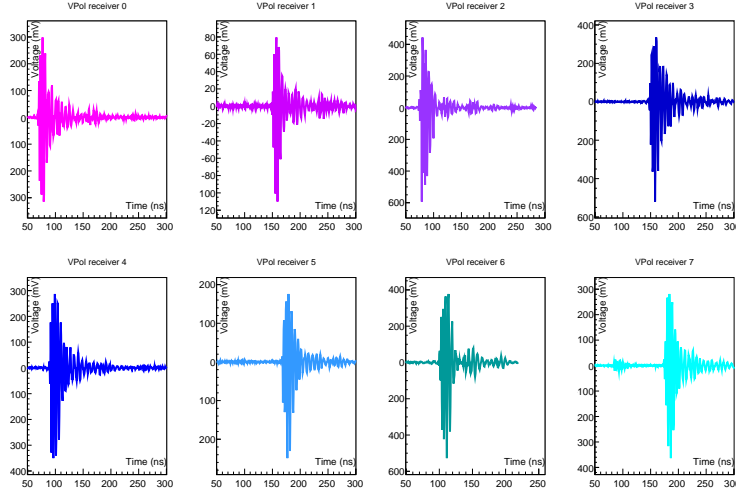


Figure 3: ARA-2 VPol response to the local, VPol calibration pulser, shown for the eight vertically-polarized (VPol) channels. HPol signals (not shown) show only noise for these events.

ARIANNA[14], located on the Ross Ice Shelf, features an isolated, radio-quiet site with log-periodic dipole antennas deployed on the surface. Downward-pointing antennas search for upcoming Askaryan signal generated by neutrino interactions in the ice; upward-pointing antennas have been used to measure down-coming Askaryan-like ‘geomagnetic’ signals generated by charged cosmic rays interacting in the Earth’s atmosphere[15]. The ANITA experiment[16] features a suite of radio-frequency horn antennas suspended from a balloon flying at an elevation of 38 km in a circumpolar orbit over the Antarctic continent, scanning for upcoming radio signals resulting from charged cosmic ray or neutrino interactions.

2. Geometric Optics and Ray tracing

The sensitivity of any neutrino-search experiment such as ARA depends on a) the degree of signal absorption in the target ice medium (determined by the imaginary component of the ice dielectric permittivity), and b) the volume of ice ‘visible’ to the radio receiver array (determined by the real component of the ice dielectric permittivity). The absorption length for RF signals in the frequency range of interest (100–1000 MHz) has been measured to exceed one km in the upper 1.5 km of the South Polar ice sheet, making it an ideal medium for neutrino detection[17]. However, the changing density of the ice results in a group velocity varying monotonically with depth. In such a case, Fermat’s Least-time principle implies that a) rays will follow curved paths, and b) there may be regions which are ‘shadowed’, for which the superposition of all contributing rays gives zero net amplitude. Moreover, there may be multiple signals observed from a single source, resulting from either continuous refraction through the ice itself, or reflection from the upper ice/air interface as illustrated in Figure 4.

The index-of-refraction should itself roughly scale with the local ice density. Robin suggested the parameterization $n(z)=1+0.86\rho(z)$ [18] based on a clever interferometric technique, in which signals recorded on the surface from a transmitter lowered into a Devon Island ice bore hole were mixed with a fixed frequency; the wavelength of the ice at the depth of the transmitter was then inferred from the measured beats. Similar parameterizations can be found elsewhere ($n(z)=0.992+0.848\rho(z)$, e.g., as determined from a fit to McMurdo Sound ice measurements[19]), although not all obey the expectation that $n(z)\rightarrow 1$ in the limit of $\rho=0$.

In a recent companion publication, also addressing the question of the index-of-refraction profile at the South Pole and elsewhere on the Antarctic continent, the general refractive index form is derived from Fermat’s Least Time

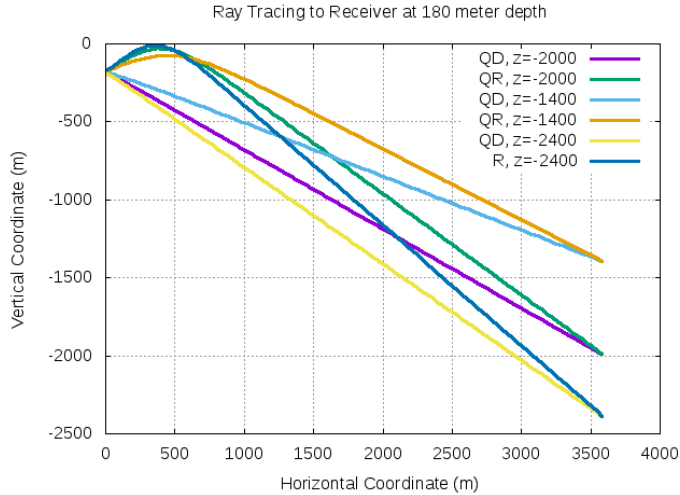


Figure 4: Simulation of ray tracing assuming ARA index-of-refraction profile with depth ($n(z)=1.78-0.43\exp(13.2z)$), showing trajectories of Quasi-Direct (QD), Quasi-Reflected (QR) rays and surface-reflected (R) rays as a function of lateral distance (x , in meters) and vertical distance (z , in meters). Signals are modeled from three possible source depths (1400m, 2000m, or 2400m) 3600m laterally displaced from a receiver 180m deep. Refracted and direct rays are typically separated by approximately 40 degrees at the measurement point with corresponding launch angles at the source separated by ~ 5 degrees. By comparison, (QD,QR) launch angle separations for neutrino interactions are limited to two degrees. Note shadow zones in upper right of plot.

principle[20]. Also presented in that reference are fits to the density data and the inferred best-fit parameters. We note that the density data at South Pole show considerable variations from experiment-to-experiment, as well as considerable deviations from smoothness, which could, in principle, result in sub-dominant ‘channeling’ effects. This possibility is especially interesting in the context of reports of horizontal propagation of in-ice RF signals emanating from within the ‘shadow zone’ expected in the presence of a gradient to the index of refraction[21, 22, 20, 23]. Such propagation could occur if there are density layers in the firn. A density inversion could produce a horizontal waveguide where radiation is confined by refraction, similar to an optical fiber with a graded index of refraction. Similarly, weak discontinuities in density can result in scattering surfaces for highly inclined rays, producing a “channel” for horizontal propagation.

2.1. Deep pulser broadcasts to the ARA array

In the middle of the expected cosmogenic neutrino energy spectrum ($E_\nu \sim 10^{18.5}$ eV), ARA is designed to detect sources several km distant. It is therefore critical to understand the properties of the ice within the array, especially at the 1-2 km depths corresponding to the regime over which the bulk of detectable neutrinos are expected to interact. Anticipating this, during the last year (2010-11) of IceCube construction, two pulsers were deployed on IceCube string 1 at depths $z=-1400$ m and $z=-2450$ m (“ICS1” and “ICD1”, respectively), and one on IceCube string 22 (“ICS22”) at a depth $z=-1400$ m, proximal to the planned ARA. The pulser at 2450 m depth was operated in conjunction with the ARA TestBed to validate the South Pole index of refraction profile with depth $n(z)$ and also the RF attenuation dependence on depth[10], but failed within the first year of operation. The pulsers at depths of 1400 m were operated in 2014/15 as part of the calibration of ARA-2 and ARA-3, and again in 2016/17 after the ARA-2 trigger timing and readout window was adjusted, enabling capture of an extended waveform.

Given the monotonic increase of $n(z)$ with depth over the upper 150 meters of the ice sheet, the presence of two rays from source to receiver is generic for our geometry (Fig. 4), with a quasi-direct (QD) ray typically upcoming at the station and either a reflected or a quasi-reflected ray (“QR”, cresting prior to “true” reflection at the upper surface) downgoing. The maximum in-ice height of the QR ray can be determined from Snell’s law and either the launch angle of the ray at the source, or the received angle at the station. The time delay between arrival of the QD and the QR rays is of order hundreds of ns; with the exception of the 2016/17 ARA-2 data, this time lag is generally larger than the waveform capture window.

2.2. Analysis of QD and QR rays

Figures 5 and 6 show deep pulser events which trigger ARA-2 and ARA-3, respectively. The QD rays travel exclusively through deep ice; the sharpness of their leading edge implies relatively little scattering and/or dispersive effects, consistent with studies of vertical echoes[24]. By contrast, the pulses identified as QR rays suggest a precursor which, we speculate, may be due to scattering in the firn layer near the top of the pulse trajectory. The somewhat irregular signal shapes from the deep pulser have been considered in a previous article[10]. In addition to evident saturation of the front-end amplifiers, resulting in compression and signal dilation, we speculate that the transmitters

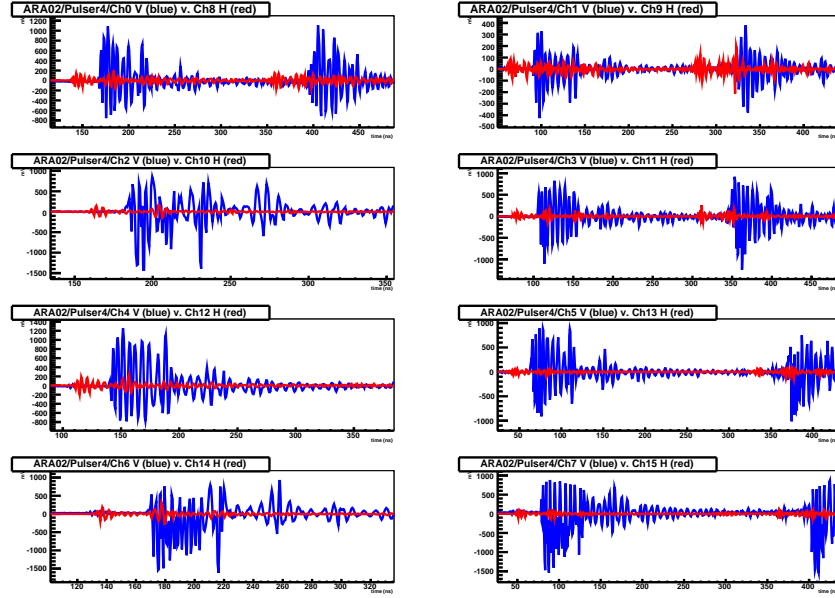


Figure 5: ICS1 waveform captures registered by ARA-2 station showing 16 channels in 8 H/V co-located pairs (blue=VPol [Channels 0–7]; red=HPol [Channels 8–15], with significantly smaller amplitude). The QD and QR signals, separated by hundreds of ns, are clearly evident in five of the eight panels. We also observe a time advance of the lower-amplitude HPol channels (red) relative to the VPol channels.

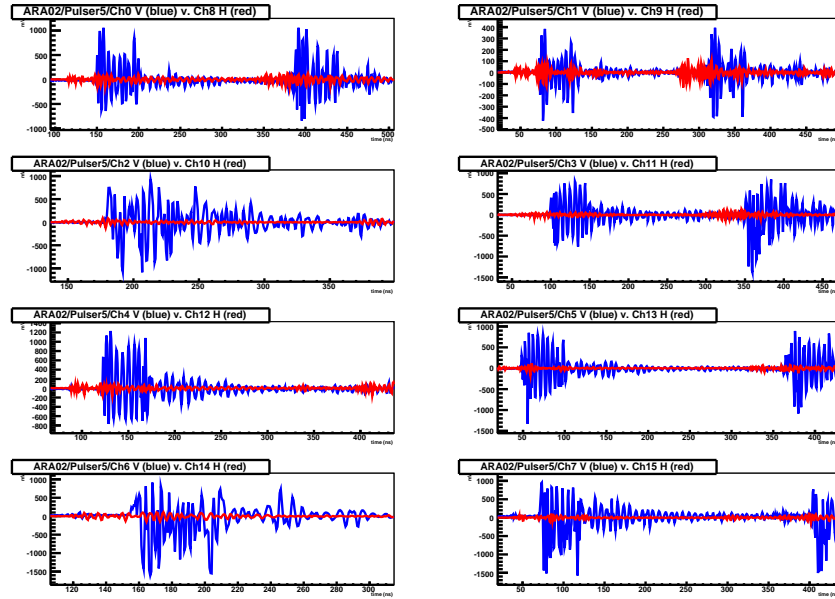


Figure 6: ICS22 waveform captures registered by ARA-2 station showing 16 channels in 8 H/V pairs (blue=VPol [Channels 0–7]; red=HPol [Channels 8–15]).

may have suffered damage after deployment¹, resulting in imperfect coupling of the transmitter itself to the antenna used to broadcast the signal. Such imperfect coupling can result in loss of fidelity, as well as enhanced cross-polarization gain.

The observed received HPol signals, having magnitude $\sim 5\text{--}10\%$ relative to VPol, from the nominally deep VPol transmitters is somewhat unexpected. In addition to possible HPol emission at the source, such an effect might arise from (at least) two sources, in isolation or in combination:

- cross-talk at the electronics level between VPol and HPol DAQ electronics traces, and/or mutual inductance between the receiver antennas (the fact that the HPol antennas are in the null of the VPol beam pattern notwithstanding), and/or cross-polarized VPol response from a dominantly HPol receiver antenna, all of which should lead to observed H/V signals which are simultaneous in time. This is, however, inconsistent with observations of local in-ice VPol calibration pulser transmitter signals, at distances of approximately 30-50 meters from the receiver array, which show no evident HPol signals comparable to those observed here.
- An ice-related effect, including:
 - Inclined conducting layers within the ice, which act as an *in situ* polarizer.
 - “circular” birefringence, for which the birefringence basis is Left Circular Polarization vs. Right Circular Polarization, and which could “rotate” a pure VPol signal at the source to a mixture of VPol and HPol, resulting in, on average, an equal admixture of VPol and HPol propagating signals. The actual relative strengths of the two components would roughly vary linearly with distance. The fact that the HPol/VPol received signal amplitudes appear to be more-or-less constant, in all channels, for all receiver stations, disfavors this hypothesis.
 - “linear” birefringence, in which the signal projects onto two (presumably perpendicular) propagation axes, referred to as the “ordinary” (“O”, with a refractive index n_O and a ‘fast’ propagation velocity c_0/n_O , with c_0 the vacuum velocity of light) or “extra-ordinary” (“E”, with a ‘slow’ propagation velocity c_0/n_E) axes. Upon arrival at the receiver, each of the O and E signals then project back onto the receiver antenna axis, resulting in an expected doublet of signals for both V or H, with amplitude dependent on the inclination angle of the underlying birefringent basis relative to “true” horizontal/vertical, and a separation time dependent on the magnitude of the $n_O - n_E$ difference.

We consider the last of these hypotheses in more detail in Section 3.

2.2.1. Comparison of observed D-R time difference against model

The observed QD/QR time delays can be used to discriminate between putative $n(z)$ models. Several functional $n(z)$ forms were tested against the measured timings. These included:

- Krav04: $n(z)=1.37-(4.6z+13.72z^2)$ for $z > -0.18$ km, as suggested by a polynomial fit to direct radio wavespeed measurements at South Pole[25].
- Model 2: $n(z)=0.8+0.98/(1+\exp(30z))$
- ARA: $n(z)=1.78-0.43\exp(13.2z)$,

with z in units of km, and increasingly negative with increasing depth. The last two exponential forms match the density dependence expected in a gravitational field. For each putative model, we calculate the sum, over all 16 ARA channels, of the squared deviation between the measured (QR,QD) arrival time difference, and the time difference predicted by a ray tracing model, assuming a given $n(z)$ form, as shown in Table 1. We find that the profile $n(z)=1.78-0.43\exp(13.2z)$ currently used in the ARA Monte Carlo simulation provides the best fit to both the available density data (presented in [20]), and also to the measured time differences between the QR and QD rays, observed in our experimental data. This functional form also matches the $n_{surface}(z=0)=1.35$ and $n_{deep}(z<-0.2)\rightarrow 1.78$ boundary conditions, consistent with density measurements at the South Pole.

Channel-by-channel, Figure 7 compares the calculated, expected time difference between the arrival of the QD and QR rays using our putative $n(z)$ model (the default ARA model) with data. Given the inherent uncertainty in discerning hit times algorithmically, the two show acceptable agreement.

2.3. QD vs. QR zenith angle direction reconstruction

The pre-saturation leading-edges of the received waveforms are adequate to infer source timing, and therefore source location reconstruction. Using the calibrated station geometry, one can calculate the zenith angle of the arriving rays and verify their consistency with the QR/QD arrival-angle hypothesis. For this reconstruction, we determine the incidence angles for the set of all QD rays, and the set of all QR rays, separately and independently. As shown in

¹Unfortunately, the cross-polarization characteristics of the transmitter were not measured prior to deployment.

ARA station	Functional Form	$\Sigma(\delta_t^{QD-QR}(Model - Data))^2 (ns^2)$ (IC22S/IC1S)
2	Krav04	652230/1378220
2	Model 2	576483/1014030
2	ARA	61752/23360
3	Krav04	1099209/487622
3	Model 2	974600/391978
3	ARA	72309/43107

Table 1: Comparison of index-of-refraction model predictions to measured QD-QR time differences. Numbers in third column represent sum, over all channels, of squares of differences between model-predicted (QD,QR) time difference relative to measurement, for IC22S and IC1S double pulses, respectively.

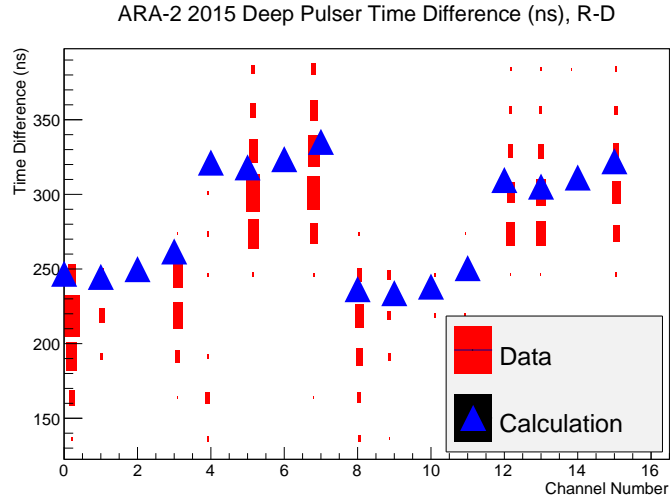


Figure 7: Measured time differences between QD and QR rays for ARA-2 2017 deep pulsar data, compared with calculation.

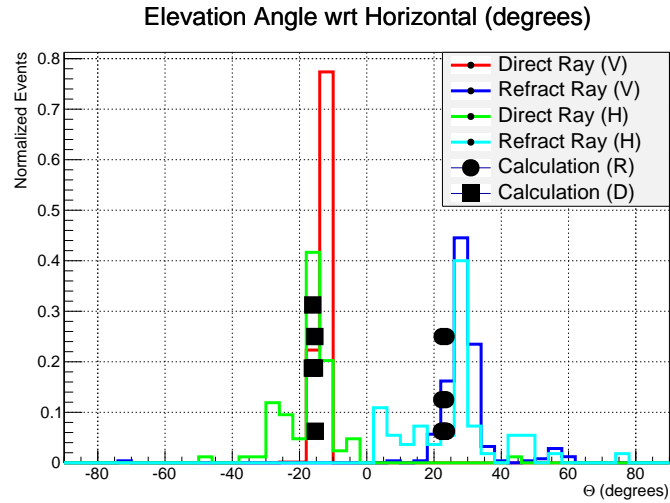


Figure 8: Calculated zenith angle of incidence, relative to horizontal, for ARA-2 2017 deep pulsar data. Histograms show the measured incidence angles for the QD and QR rays for both VPol (red for QD and blue for QR) and HPol (green for QD and cyan for QR) receiver channels. Points overlaid show expectation from model simulation, based on ARA index-of-refraction profile. We note an approximately 40 degree difference between reception angle for QD vs. QR.

Figure 8, the earlier QD set of pulses arrive from below the horizontal; the later QR set of pulses arrive from above the horizontal, consistent with expectations for the QD and QR rays, respectively.

2.4. Source Reconstruction in both Azimuth and Elevation

The standard ARA interferometry-based analysis event reconstruction[10] cross-correlates the waveforms (QD_i , QD_j), where QD_i and QD_j are the quasi-direct signals on channels i and j . Through a fast lookup table of calculated, expected arrival times, a set of predicted δt_{ij} (r, θ, ϕ) are produced for every possible source position. These are used to sample the Hilbert envelope of the i - j cross correlation function and give weights to the putative δt_{ij} [26]. For this particular study, a second table for QR signal arrival times is built, and the cross correlation is extended to include all the available QR signals. Thus, the full reconstruction incorporates contributions from all possible QD-QD, QD-QR, and QR-QR pairs, and assesses the consistency of a putative 1 square degree source position in the sky with the ensemble of observed QD and QR hit times. The source location map constructed for a deep pulsar event is show in Figure 9; the brightest $1^\circ \times 1^\circ$ pixel in that map is identified as the best-fit source position. The distribution of reconstructed deep pulsar directions, as defined by the maximum intensity pixel in each event, is presented in Figures 10 and 11. In general, we reconstruct the source direction with accuracy 1–2 degrees in both azimuth and elevation.

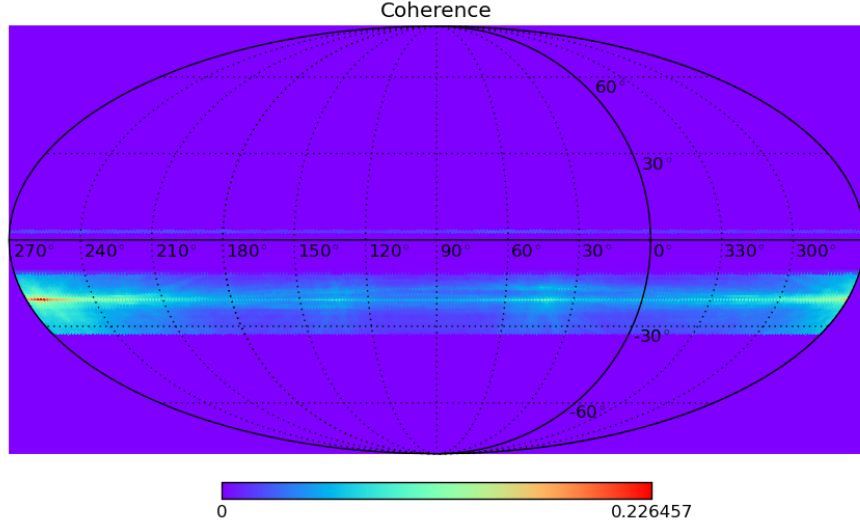


Figure 9: Reconstructed interferometric image of ARA ICS22 deep pulsar, using standard azimuth (horizontal) vs. zenith (i.e., elevation [vertical]) coordinates. Highest intensity pixel is visible in lower left.

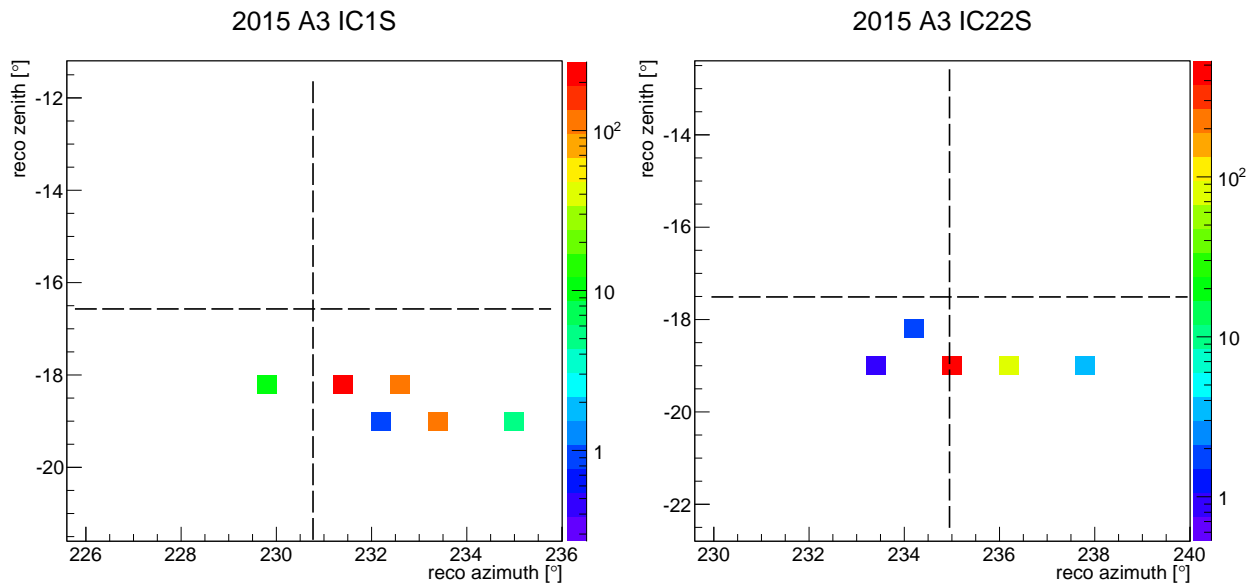


Figure 10: ARA-3 azimuthal (ϕ) vs. zenith (θ) reconstructed source locations during time when ICS1 (left) and ICS22 (right) was pulsing. Dashed lines indicate “true” source location. There are two and zero outliers, respectively, not shown, beyond the plot boundaries.

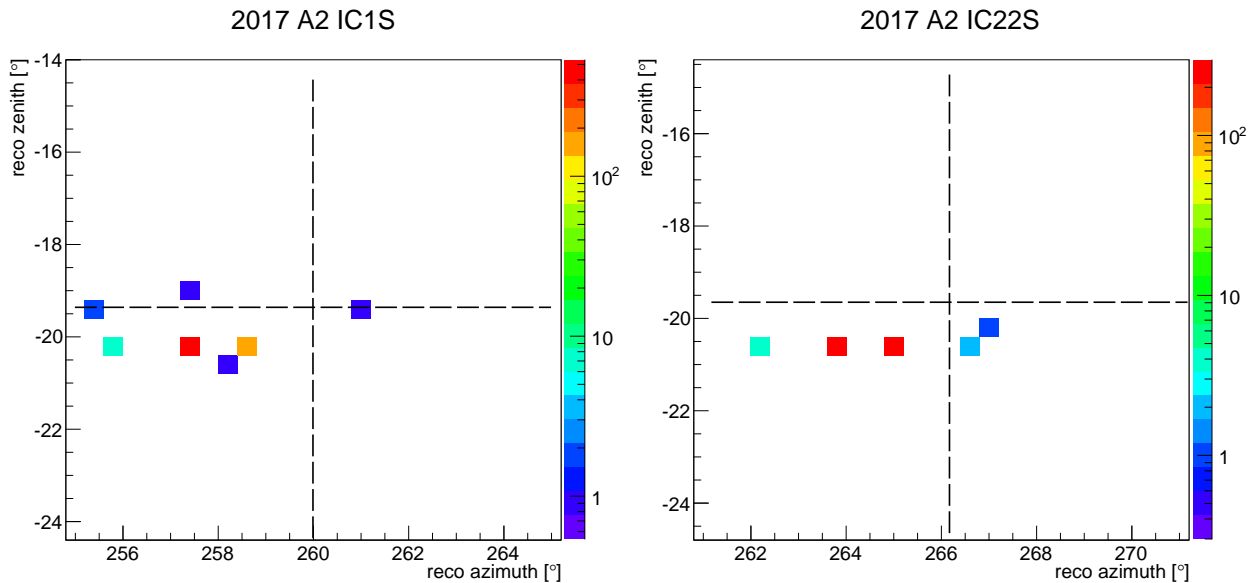


Figure 11: ARA-2 azimuthal (ϕ) vs. zenith (θ) reconstructed source locations during time when IC1S (left) and ICS22 (right) were pulsing. There are 11 and 9 outliers, respectively, not shown, beyond the plot boundaries.

2.5. Range Reconstruction

The reconstruction from QD rays permits a good direction to the vertex, but determining the distance to the vertex is more difficult, as (absent additional QR information) this requires a determination of the curvature of the radiation front, which is limited by both the modest 20 m baseline of the station and the inherent signal arrival time resolution. There is ~ 100 ps resolution in the time-difference between hit times, as determined by waveform cross-correlations. If the antenna locations, the index-of-refraction profile, individual channel cable delays and antenna group delays were all exactly known, the wavefront reconstruction would be entirely determined by this 100 ps timescale. Unfortunately, there are significant uncertainties in all of these quantities, which have a combined error at least an order of magnitude larger than the 100 ps timescale.

In the case where both the QD and QR signals are observed, however, comparison of the QD with the QR signal arrival times allows improved estimation of range-to-vertex without use of wavefront curvature information. Considering the quasi-reflected ray as if it were detected by an “image” station above the ice surface, for a 200m deep receiver, the baseline for reconstruction by both rays is of order twice the depth of the station, or 400m, enabling a full 3D reconstruction.

Similar to the procedure followed for interferometric reconstruction of azimuth and elevation, we can empirically determine the source range most consistent with the observed QD-QR time difference. The results of this exercise are presented in Figure 12 for ARA-2 reconstruction of the ICS1 and ICS22 pulsers. We observe that deviations in elevation reconstruction of order one degree typically translate into range errors of tens of percent. Table 2 summarizes our results numerically, and indicates that we can use the time difference between QD and QR signals to estimate the range to within $\sim 15\%$.

Station/Source	Nominal/Reconstructed		
	θ (deg)	ϕ (deg)	r (m) (deviation)
A2/IC1S	-19.36/- 20.19 ± 0.07	259.99/ 257.6 ± 0.56	3666 ± 543 / 4215 (+15%)
A2/IC22S	-19.65/- 20.64 ± 0.02	266.17/ 264.4 ± 0.64	3609 ± 530 / 4896 (+36%)
A3/IC1S	-16.57/- 18.21 ± 0.35	230.77/ 232.2 ± 0.95	4269 ± 696 / 4711 (+10%)
A3/IC22S	-17.51/- 18.9 ± 0.05	234.95/ 235.2 ± 0.45	4040 ± 603 / 4298 (+6%)

Table 2: Summary of reconstructed deep pulser source locations compared with “known” source location. For each pair presented, the first value represents the nominal (‘true’) value; the second value (in bold) represents the value our source reconstruction algorithm returns, along with the associated statistical error.

3. Study of H/V relative signal timing and evidence for birefringence

The pathlengths from the ICS1 and ICS22 transmitters to the ARA receiver stations is of order 3–5 km, along a predominantly horizontal trajectory. To our knowledge, this is the longest horizontal baseline used for testing electro-

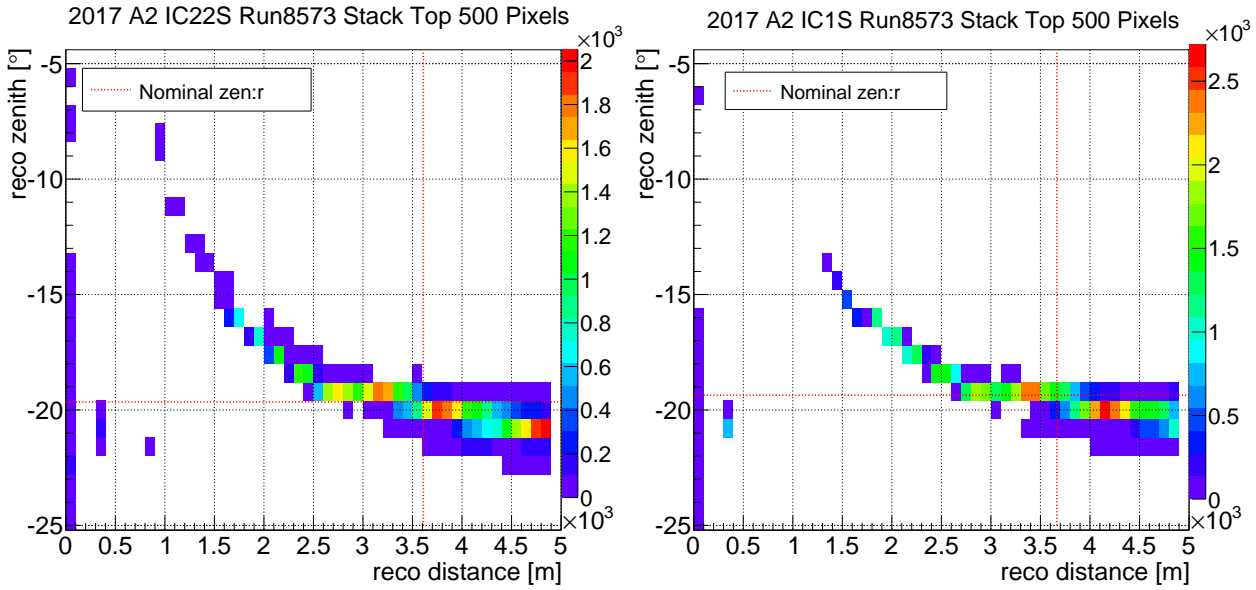


Figure 12: ARA-2 “stacked” pixels range vs. elevation(θ) distribution. Ranking by source likelihood, we plot the (range, θ) of the highest 500 pixels of each event. Shown is this stacked distribution from events during time when IC22S was pulsing. The color intensity scale indicates the frequency of a putative (range, θ) point.

magnetic signal propagation, of any type, in the polar regions. As such, this provides a singular opportunity to probe the wavespeed variation with polarization. As shown in Figures 5 and 6, and zoomed for two ARA-2 channels in Figure 13, the HPol signal from the deep pulsers is clearly advanced by 20–30 ns, for both ARA-2 and ARA-3, relative to the signal registered in the co-located VPol receiver. Since the elevation angles of the signal arrival are within ~ 20 degrees of horizontal (Figure 8), the expected signal arrival times should be nearly identical for this H/V channel pair.

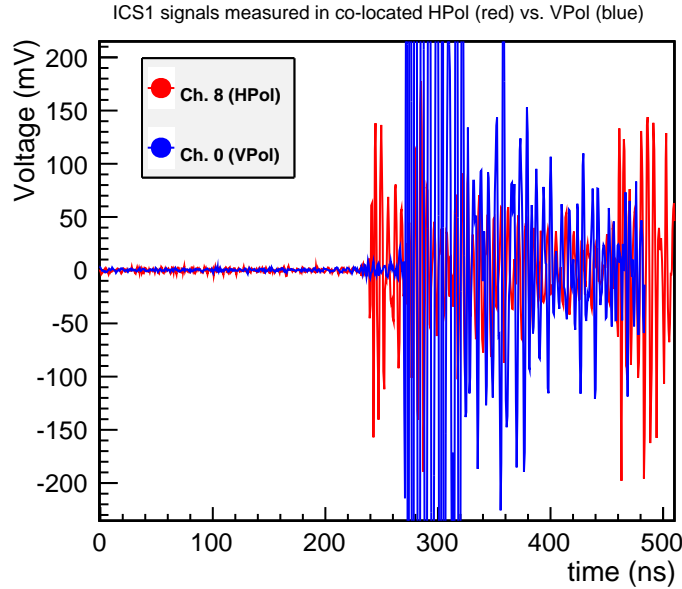


Figure 13: Zoom of channels 0 (VPol) and 8 (co-located HPol) for signals received from IC1S, illustrating time difference between HPol and VPol waveforms.

Given that ice crystals are known to exhibit linear, but not circular birefringence[27], we consider the arrival of the HPol signals prior to the arrival of the VPol signals to be most plausibly explained by linear ice birefringence, although this requires some bulk ice crystal alignment. In the absence of any ice crystal directional asymmetry, one would expect the radio-frequency wavespeed to be uniform in all directions. Isotropy of the Antarctic ice sheet is broken in two directions – vertically, due to the gradient in hydrostatic pressure with depth and resulting in a compressional stress on ice crystals, and horizontally, due to the local ice flow direction and resulting in a torsional strain, and therefore, a preferred axis laterally.

To calculate the magnitude of the birefringent asymmetry between H/V pairs in data, we must correct for the 2–3 meter shallower deployment depth of the H-pol antenna of the pair, leading to a timing correction $\delta t_i^{corr} \approx n(z)\delta z(\sin\theta_i)/c_0$,

with δz the vertical separation of the HPol vs. VPol receivers, θ_i the ray incidence angle relative to the horizontal, $n(z)$ the local index-of-refraction, and c_0 the velocity of light in vacuum. After applying this correction, the calculated HPol advance relative to same-string VPol channels is summarized in Figure 14, for deep pulser signals observed in ARA-2 and ARA-3. In the Figure, the horizontal value corresponds to the i^{th} VPol receiver channel; the y-value gives the measured time difference, after correction, relative to the zero birefringence expectation, for the nearest HPol channel. We note that prior to the vertical-displacement correction described above, the ARA-2 and ARA-3 δ_t^{V-H} values are

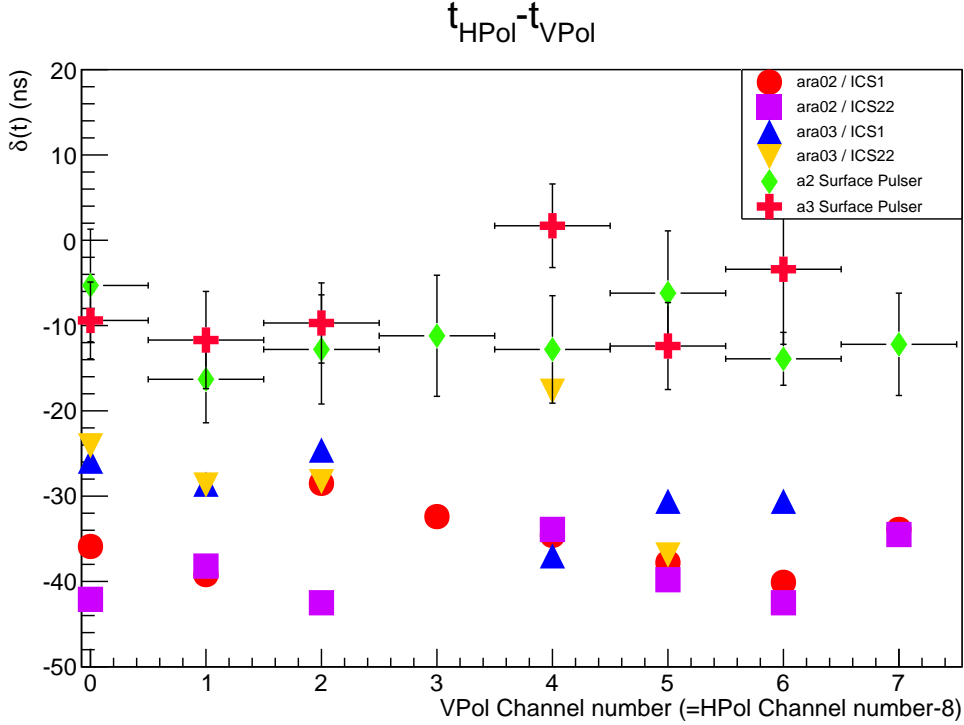


Figure 14: δ_t^{V-H} ARA-2 and ARA-3 data. x-axis refers to channel number of vertically-polarized receiver; y-value gives the (corrected) time difference between registered signal arrival time on the co-located HPol channel for that hole/station relative to registered VPol signal arrival time for an H/V pair. For comparison, results from a surface transmitter survey, at lateral distances 100–200 meters from each station, are also shown. In the absence of birefringence and/or timing miscalibration, all data points should approximately lie on the x-axis, consistent with zero propagation-time difference. We observe that ARA-2 has typical time differences of 30–40 ns relative to a propagation time of approximately 20 μs ; for ARA-3, values are approximately 5–10 ns smaller. Systematic errors on ARA2 and ARA3 H/V time differences are indicated by surface pulser survey data, and estimated at 3–4 ns.

consistent with each other; after correction, the value of δ_t^{V-H} (ARA-3) is typically 15–20% smaller than for ARA-2, despite the fact that the propagation distance from the deep pulsers to the ARA-3 station is approximately 15% longer. A simple explanation for this is, of course, that the H-V pair vertical separations have been mis-tabulated by ~ 1.5 meters. Alternately, in the birefringent model, this result may suggest that the vector from the deep pulsers to ARA-2 is more aligned with the underlying birefringent basis than ARA-3. Geometrically, the line from IC1 to ARA-2 is very nearly directly perpendicular to the horizontal ice flow direction; the line from IC1 to ARA-3 is offset by ~ 30 degrees relative to that line (Figure 2).

3.1. Cross-checks

Aside from birefringence, the observed time delay between the arrival of the HPol vs. VPol signals could, in principle, be due to a simple mis-calibration of the HPol vs. VPol receivers. To test this, we considered data taken during an RF survey of stations 2 and 3 for which a surface transmitter was broadcast from a dipole, with its long axis inclined at an angle of 45 degrees relative to vertical, within 200 m laterally of each station. Given the transmitter inclination angle, these data should have roughly equal amounts of HPol and VPol broadcast signal. We observe in Figure 14 an offset between H and V of approximately -5 – -10 ns, consistent in sign, but of somewhat smaller magnitude than we observe for broadcasts from the deep pulsers.² From inspection of the waveforms themselves, we observe a sharper rise time for the VPol signals, which we attribute to the smaller bandwidth of the HPol antennas compared to VPol antennas; however, this effect should have the result of staggering, rather than advancing the peaks of the HPol signals relative to VPol. Therefore, pending additional investigation, we interpret these data as conditional evidence for birefringence for signals propagating from the ~ 1450 -m deep pulsers.

²This effect is, in principle, consistent with horizontal birefringence through the upper firn layer of the ice sheet.

The evidence for birefringence must be interpreted in the context of previous results. The RICE Collaboration observed birefringence in vertical propagation of rays which reflect off the bedrock[24]. They conclude that the time delays accumulate mostly in the deep ice, below about 1200 m, as they observe no evidence for birefringence in the upper ice. This is consistent with a crystal orientation fabric (COF) determined by shear in the ice flow[28], which is rather modest in the upper ice. The current results, however, suggest that the upper ice does exhibit birefringence for horizontal propagation. If the COF of the upper ice is dominated by gravity, then a vertical ray would not exhibit birefringence, but a horizontal ray would since the Vpol would be along the net c -axis while Hpol would be transverse to it.

4. Conclusions and Discussion

As shown herein, the time difference between the registration of direct vs. refracted (or reflected) rays permits an estimate of the range-to-vertex, once the azimuth and elevation of an incident signal has been determined through interferometry. Additionally, if the time delay between signal arrival times for HPol vs. VPol receivers (δ_t^{V-H}) can be quantified for all geometries, then an additional constraint on the event geometry may be afforded by the measured magnitude of birefringent time difference.

At South Pole, the ARA strategy thus far has been based on receiver deployment at approximately 200 meters. In evaluating the optimal depth to site a future radio receiver array, one must consider the following:

- The launch angle difference between the QD and the QR rays increases as the receiver depth z_{Rx} also increases. The data presented here are based on reception of signals from an in-ice transmitter dipole with a very broad beam pattern, however, the Cherenkov cone from a neutrino has only a 1–2 degree transverse thickness.
- As the receiver depth z_{Rx} increases to 200 meters, the measured time difference between reception of the QD and the QR rays also increases, approaching one microsecond, and therefore requiring $\sim 2\mu s$ of data buffering, per channel, to ensure capturing both the QD and the QR rays.

These considerations, combined with the logistical overhead associated with drilling ice-holes down to 200 meters, suggest that a shallow receiver array, deployed at a depth of 25–50 meters may retain high efficiency for observation of the QD and QR rays from a neutrino interaction, have good (of order hundreds of meters) range resolution, and sufficient timing resolution to measure δ_t^{V-H} (giving a redundant measure of range-to-vertex) within a tight (512 ns) waveform capture time window.

The observations presented here are a small part of the radio-glaciological data needed to fully characterize RF propagation of relevance to the ARA experiment. In this regard, within the last two years, a 1700-m deep ice core, 0.5–several km from current ARA stations, was extracted from the South Pole ice[29]. With the consent of the NSF, a piezo-electric technology radio-frequency transmitter, based on the same model as that employed in the balloon-borne HiCal experiment[30], was used in January, 2018 to sample the upper 800 meters of the SPICE borehole. The beam pattern of that transmitter is somewhat more isotropic than that used in the deep pulser studies described herein, and, by design, contains significant HPol as well as VPol content. Those data are currently under analysis. In parallel, we are working to develop a first-principles model, based on measurements of the crystal orientation fabric, that absolutely predicts, for any polarization and k -vector, an observed birefringent asymmetry.

5. Acknowledgments

We thank the National Science Foundation for their generous support through Grant NSF OPP-1002483 and Grant NSF OPP-1359535. We further thank the Taiwan National Science Councils Vanguard Program: NSC 102-2628-M-002-010 and the Belgian F.R.S.-FNRS Grant4.4508.01. We are grateful to the U.S. National Science Foundation-Office of Polar Programs and the U.S. National Science Foundation-Physics Division. We also thank the University of Wisconsin Alumni Research Foundation, the University of Maryland and the Ohio State University for their support. Furthermore, we are grateful to the Raytheon Polar Services Corporation and the Antarctic Support Contractor, for field support. A. Connolly thanks the National Science Foundation for their support through CAREER award 1255557, and also the Ohio Supercomputer Center. K. Hoffman likewise thanks the National Science Foundation for their support through CAREER award 0847658. A. Connolly, H. Landsman, and D. Besson thank the United States-Israel Binational Science Foundation for their support through Grant 2012077. A. Connolly, A. Karle, and J. Kelley thank the National Science Foundation for the support through BIGDATA Grant 1250720. B. A. Clark thanks the National Science Foundation for support through the Graduate Research Fellowship Program Award DGE-1343012. D. Besson and A. Novikov acknowledge support from National Research Nuclear University MEPhi (Moscow Engineering Physics Institute). R. Nichol thanks the Leverhulme Trust for their support.

References

- [1] G. Askaryan. Excess negative charge of an electron-photon shower and its coherent radio emission. *Soviet Physics JETP*, 14:441–443, 1962.
- [2] G. A. Askaryan. Excess negative charge of electron-photon shower and the coherent radiation originating from it. radiorecording of showers under the ground and on the moon. *J. Phys. Soc. Japan*, Vol. 17, Suppl. A-III:257, 1962.
- [3] G. A. Askaryan. Coherent Radio Emission from Cosmic Showers in Air and in Dense Media. *Soviet Phys. JETP*, 21:658, 1965.
- [4] Francis Halzen. High-energy neutrino astrophysics. *Nature Physics*, 13(3):232–238, 2017.
- [5] Ralph Engel, David Seckel, and Todor Stanev. Neutrinos from propagation of ultrahigh energy protons. *Physical Review D*, 64(9):093010, 2001.
- [6] Kumiko Kotera, Denis Allard, and Angela V Olinto. Cosmogenic neutrinos: parameter space and detectability from PeV to ZeV. *Journal of Cosmology and Astroparticle Physics*, 2010(10):013, 2010.
- [7] Markus Ahlers and Francis Halzen. Minimal cosmogenic neutrinos. *Physical Review D*, 86(8):083010, 2012.
- [8] Katsuaki Asano and Peter Mszros. Ultrahigh-energy cosmic ray production by turbulence in gamma-ray burst jets and cosmogenic neutrinos. *Phys. Rev.*, D94(2):023005, 2016.
- [9] IceCube Collaboration et al. Multimessenger observations of a flaring blazar coincident with high-energy neutrino icecube-170922a. *Science*, 361(6398):eaat1378, 2018.
- [10] P. Allison and J. Auffenberg and R. Bard and J. J. Beatty and D. Z. Besson and S. Boeser and C. Chen and P. Chen and A. Connolly and J. Davies and M. DuVernois and B. Fox and P. W. Gorham and E. W. Grashorn and K. Hanson and J. Haugen and K. Helbing and B. Hill and K. D. Hoffman and M. Huang and M. H. A. Huang and A. Ishihara and A. Karle and D. Kennedy and H. Landsman and A. Landrie and T. C. Liu and L. Macchiarulo and K. Mase and T. Meures and R. Meyhandan and C. Miki and R. Morse and M. Newcomb and R. J. Nichol and K. Ratzlaff and M. Richman and L. Ritter and B. Rotter and P. Sandstrom and D. Seckel and J. Touart and G. S. Varner and M.-Z. Wang and C. Weaver and A. Wendorff and S. Yoshida and R. Young. Design and initial performance of the Askaryan Radio Array prototype EeV neutrino detector at the South Pole. *Astroparticle Physics*, 35(7):457–477, 2012.
- [11] P. Allison, J. Auffenberg, R. Bard, J. J. Beatty, D. Z. Besson, C. Bora, C.-C. Chen, P. Chen, A. Connolly, J. P. Davies, M. A. DuVernois, B. Fox, P. W. Gorham, K. Hanson, B. Hill, K. D. Hoffman, E. Hong, L.-C. Hu, A. Ishihara, A. Karle, J. Kelley, I. Kravchenko, H. Landsman, A. Landrie, C.-J. Li, T. Liu, M.-Y. Lu, R. Maunu, K. Mase, T. Meures, C. Miki, J. Nam, R. J. Nichol, G. Nir, A. O’Murchadha, C. G. Pfendner, K. Ratzlaff, M. Richman, B. Rotter, P. Sandstrom, D. Seckel, A. Shultz, J. Stockham, M. Stockham, M. Sullivan, J. Touart, H.-Y. Tu, G. S. Varner, S. Yoshida, and R. Young. First constraints on the ultra-high energy neutrino flux from a prototype station of the Askaryan Radio Array. *Astroparticle Physics*, 70:62–80, 2015.
- [12] P. Allison, R. Bard, J. J. Beatty, D. Z. Besson, C. Bora, C.-C. Chen, C.-H. Chen, P. Chen, A. Christenson, A. Connolly, J. Davies, M. Duvernois, B. Fox, R. Gaior, P. W. Gorham, K. Hanson, J. Haugen, B. Hill, K. D. Hoffman, E. Hong, S.-Y. Hsu, L. Hu, J.-J. Huang, M.-H. A. Huang, A. Ishihara, A. Karle, J. L. Kelley, D. Kennedy, I. Kravchenko, T. Kuwabara, H. Landsman, A. Landrie, C.-J. Li, T. C. Liu, M.-Y. Lu, L. Macchiarulo, K. Mase, T. Meures, R. Meyhandan, C. Miki, R. Morse, J. Nam, R. J. Nichol, G. Nir, A. Novikov, A. O’Murchadha, C. Pfendner, K. Ratzlaff, M. Relich, M. Richman, L. Ritter, B. Rotter, P. Sandstrom, P. Schellin, A. Shultz, D. Seckel, Y.-S. Shiao, J. Stockham, M. Stockham, J. Touart, G. S. Varner, M.-Z. Wang, S.-H. Wang, Y. Yang, S. Yoshida, and R. Young. Performance of two Askaryan Radio Array stations and first results in the search for ultrahigh energy neutrinos. *Physical Review D*, 93(8):082003, 2016.
- [13] AG Viereg, K Bechtol, and A Romero-Wolf. A technique for detection of PeV neutrinos using a phased radio array. *Journal of Cosmology and Astroparticle Physics*, 2016(02):005, 2016.
- [14] S. W. Barwick and E. C. Berg and D. Z. Besson and E. Cheim and T. Duffin and J. C. Hanson and S. R. Klein and S. A. Kleinfelder and T. Prakash and M. Piasecki and K. Ratzlaff and C. Reed and M. Roumi and A. Samanta and T. Stezelberger and J. Tatar and J. Walker and R. Young and L. Zou. Design and Performance of the ARIANNA Hexagonal Radio Array Systems. *IEEE Trans. Nucl. Sci.*, 62(5):2202–2215, 2015.
- [15] SW Barwick, DZ Besson, Alexander Burgman, E Chiem, Allan Hallgren, JC Hanson, SR Klein, SA Kleinfelder, A Nelles, C Persichilli, et al. Radio detection of air showers with the ARIANNA experiment on the Ross Ice Shelf. *Astroparticle Physics*, 90:50–68, 2017.

- [16] P. W. Gorham, P. Allison, S W. Barwick, and et al. The Antarctic Impulsive Transient Antenna ultra-high energy neutrino detector: Design, performance, and sensitivity for the 2006-2007 balloon flight. *Astropart. Phys.*, 32(1):10–41, 2009.
- [17] Barwick, S and Besson, D and Gorham, P and Saltzberg, D. South Polar in situ radio-frequency ice attenuation. *Journal of Glaciology*, 51(173):231–238, 2005.
- [18] G de Q Robin. Velocity of radio waves in ice by means of a bore-hole interferometric technique. *Journal of Glaciology*, 15(73):151–159, 1975.
- [19] Austin Kovacs, Anthony J Gow, and Rexford M Morey. A reassessment of the in-situ dielectric constant of polar firn. Technical report, COLD REGIONS RESEARCH AND ENGINEERING LAB HANOVER NH, 1993.
- [20] SW Barwick, EC Berg, DZ Besson, G Gaswint, C Glaser, A Hallgren, JC Hanson, SR Klein, S Kleinfelder, L Köpke, et al. Observation of classically forbidden electromagnetic wave propagation and implications for neutrino detection. *arXiv preprint arXiv:1804.10430*, 2018.
- [21] S.H. Wang et al. Calibration, Performance, and Cosmic Ray Detection of ARIANNA-HCR Prototype Station. In *Proceedings of the 35th ICRC, Busan, Korea*, volume 1, pages 1–8, 2017.
- [22] Jordan Hanson. *The Performance and Initial Results of the ARIANNA Prototype*. PhD thesis, University of California, Irvine, July 2013.
- [23] C Deaconu, AG Viereg, SA Wissel, J Bowen, S Chipman, A Gupta, C Miki, RJ Nichol, and D Saltzberg. Measurements and modeling of near-surface radio propagation in glacial ice and implications for neutrino experiments. *arXiv preprint arXiv:1805.12576*, 2018.
- [24] Dave Besson, Ilya Kravchenko, Andres Ramos, and Juliet Remmers. Radio Frequency Birefringence in South Polar Ice and Implications for Neutrino Reconstruction. *Astropart. Phys.*, 34:755–768, 2011.
- [25] Ilya Kravchenko, David Besson, and Josh Meyers. In situ index-of-refraction measurements of the south polar firn with the rice detector. *Journal of Glaciology*, 50(171):522–532, 2004.
- [26] M Beheler-Amass, M Beydler, A Karle, JL Kelley, and MY Lu. Interferometric Neutrino Event Reconstruction in Inhomogeneous Media with the Askaryan Radio Array. 1:1–8, 2017.
- [27] Hargreaves, ND. The radio-frequency birefringence of polar ice. *Journal of Glaciology*, 21(85):301–313, 1978.
- [28] P Buford Price, Oleg V Nagornov, Ryan Bay, Dmitry Chirkin, Yudong He, Predrag Miocinovic, Austin Richards, Kurt Woschnagg, Bruce Koci, and Victor Zagorodnov. Temperature profile for glacial ice at the South Pole: Implications for life in a nearby subglacial lake. *Proceedings of the National Academy of Sciences*, 99(12):7844–7847, 2002.
- [29] Kimberly Ann Casey, TJ Fudge, TA Neumann, EJ Steig, MGP Cavitte, and DD Blankenship. The 1500 m South Pole ice core: recovering a 40 ka environmental record. *Annals of Glaciology*, 55(68):137–146, 2014.
- [30] PW Gorham, P Allison, O Banerjee, JJ Beatty, K Belov, DZ Besson, WR Binns, V Bugaev, P Cao, C Chen, et al. Antarctic Surface Reflectivity Measurements from the ANITA-3 and HiCal-1 Experiments. *Journal of Astronomical Instrumentation*, page 1740002, 2017.